New insights on wind turbine wakes from large-eddy simulation: Wake contraction, dual nature, and temperature effects

Received: 28 April 2022 | Revised: 15 February 2023 | Accepted: 1 May 2023

DOI: 10.1002/we.2827

SPECIAL ISSUE PAPER

WILEY

New insights on wind turbine wakes from large-eddy simulation: Wake contraction, dual nature, and temperature effects

Sicheng Wu[1] | Cristina L. Archer[1] | Jeffrey D. Mirocha[2]

[1]Center for Research in Wind (CReW), University of Delaware, Newark, Delaware, USA

[2]Lawrence Livermore National Laboratory, Livermore, California, USA

Correspondence
Cristina L. Archer, Center for Research in Wind (CReW), University of Delaware, Newark, DE 19711, USA.
Email: carcher@udel.edu

Funding information
National Science Foundation, Grant/Award Number: 1564565; LLNL, Grant/Award Number: DE-AC52-07NA27344

Abstract

Large-eddy simulation (LES) has been adopted to study wind turbine wakes because it can capture fine-scale details of turbulent wind flows and interactions with wind turbines. Here, we use the LES version of the Weather Research and Forecasting (WRF) model with an actuator disk model to gain insights on several wake effects that have been traditionally difficult to measure. The first finding is that the wake has a "dual nature," meaning that the wind speed deficit behaves differently from the added turbulent kinetic energy (TKE) and the two are not co-located in space. For example, the wind speed deficit peaks at hub height and reaches the ground within 8D (D is the rotor diameter), but added TKE peaks near the rotor tip and generally remains aloft. Second, temperature changes near the ground are driven by the added TKE in the rotor area and by atmospheric stability. The combination of these two factors determines the sign and intensity of the vertical heat flux divergence below the rotor, with convergence and warming associated with stable conditions and weak divergence and modest cooling with unstable conditions. Third, wakes do not expand indefinitely, as suggested by similarity theory applied to the wind speed deficit, but eventually stop expanding and actually contract, at different rates depending on atmospheric stability. The implication of these findings is that, in order to study wakes, it is not sufficient to focus on wind speed deficit alone, because TKE is also important and yet behaves differently from the wind speed deficit.

KEYWORDS
large-eddy simulation, temperature, turbulence kinetic energy, wake expansion, wind speed deficit, wind turbine wake

1 | INTRODUCTION

Wind turbines extract kinetic energy from the wind and, as a consequence, reduce wind speed and generate turbulence in their downstream wakes. Thus, they can potentially impact local near-ground climate properties, such as temperature and moisture. Several past studies have investigated how wind turbine wakes impact near-ground properties. The first field campaigns and remote sensing studies found evidence of warming at night[1–4] and weak cooling during the day[1,2] due to wind turbine wakes. However, some remote sensing studies have also found

opposite impacts on temperature, for example, warming during the day.[2,5] Other observational studies have used atmospheric stability, rather than the simple day/night classification, to understand temperature changes. A stable atmosphere is characterized by low turbulence, a lapse rate that is smaller than the dry adiabatic, and a tendency to suppress vertical motion; vice versa, an unstable atmosphere is characterized by high turbulence, a lapse rate that is larger than the dry adiabatic, and a tendency to enhance vertical motion; lastly, a neutral atmosphere neither suppresses nor enhances vertical motion and has a lapse rate close to the dry adiabatic. Many past observational studies found warming during stable conditions and weak or no cooling in unstable conditions.[6–9] However, there exist some exceptions at times.[6] Some ground measurement studies found no significant temperature effects caused by wind turbine wakes.[10] In conclusion, there are still conflicting findings on how and by how much wind turbine wakes impact temperature near the ground.

By contrast, enhanced vertical mixing caused by the turbulent wakes is the widely accepted mechanism used to explain the temperature changes near the ground. Enhanced vertical mixing implies that the additional turbulence and the enhanced vertical fluxes found in the (upper) rotor region extend all the way down to the ground. However, there is not sufficient evidence to support that enhanced vertical mixing truly happens near the ground. As demonstrated in the VERTEX field experiment,[9,11] vertical mixing (i.e., turbulence and friction velocity) is actually reduced, instead of enhanced, near the ground, in the wake of a single wind turbine. Since no enhanced vertical mixing exists near the ground, the enhanced vertical mixing cannot be the mechanism behind the temperature change. Wu and Archer[11] proposed that the mechanism behind the temperature change near the ground is the vertical divergence of the turbulent heat fluxes below the rotor. In stable conditions, the enhanced downward heat flux in the rotor area and the reduced or unchanged heat flux near the ground cause convergence below the rotor, thus warming; vice versa, in unstable conditions a weak divergence of the heat fluxes causes weak cooling. Their hypothesis is supported by the modeling study by Xia et al,[12] who used the Weather Research and Forecasting (WRF) mesoscale model[13] and the Fitch's wind farm parameterization[14] to study the temperature changes caused by large wind farms. Although the WRF model coupled with the Fitch parameterization was able to capture the divergence/convergence mechanism, other issues suggest that a mesoscale model may not be adequate to resolve the wake turbulence accurately enough to predict temperature changes. For example, the Fitch parameterization inaccurately treats added turbulence kinetic energy (TKE) by the turbines and neglects the impact of wakes of multiple wind turbines within the same grid cell.[15,16] Considering these limitations and the fact that wakes require a grid spacing finer than 1 km, mesoscale models are not appropriate for this research, where resolving the wake turbulence is crucial.

To resolve the three-dimensional turbulence field, it is more appropriate to use the large-eddy simulation (LES) technique, which captures the three-dimensional details of turbulence, necessary for the study of turbulent mixing and temperature changes caused by wind turbine wakes. There are already several LES codes specifically designed to study wind turbine wakes, ranging from in-house codes, for example, the Wind Turbine and Turbulence Simulator (WiTTS),[17,18] to open-source packages, for example, the Simulator fOr Wind Farm Applications (SOWFA) under the OpenFOAM package.[19] Reduced wind speed near the surface (fig. 2 in Calaf et al.[20]) and reduced shear stresses below the rotor area (fig. 3 in Calaf et al[21] and fig. 4 in Calaf et al.[20]) were reported in an infinitely long wind farm simulated via LES under neutral conditions, thus supporting the lack of enhanced vertical mixing near the ground. Below the turbine rotor, LES studies found warming under both stable[22] and unstable[23] conditions, in both cases accompanied by a reduction of turbulence and vertical mixing near the ground.

The modeling system selected for this study is the WRF, which contains both an LES option (WRF-LES) and a generalized actuator disk parameterization (WRF-LES-GAD) by Mirocha et al.[24] While the effects of wind turbine wakes on temperature have not been examined in previous WRF-LES-GAD studies, the framework has been used to examine the impacts of stability on wake properties[24–26] as well as wake interactions among multiple turbines in both idealized[27] and real-world[28] conditions.

In conclusion, currently there is no consensus about how wind turbine wakes affect near-ground temperature and not enough evidence that the mechanism behind temperature changes is indeed the divergence/convergence of vertical heat fluxes. Although a wind turbine wake is a source of both a wind speed deficit and TKE, it is unclear how these two properties interact with each other and, ultimately, how to define a wind turbine wake, whether using just the wind speed deficit, or considering also the added turbulence. We refer to this issue as the "dual nature" of the wake.

This paper aims at answering the following research question: How do wind turbine wakes affect the near-ground microclimate under different stability conditions? Three aspects are going to be addressed:

1. dependency of the temperature impacts on atmospheric stability;
2. verification of the divergence/convergence mechanism; and
3. characterization of the wake properties (wind speed deficit, TKE, expansion, and contraction).

The WRF-LES-GAD model described above is used in this study under three stability conditions to address the above-mentioned issues. In addition to validating the single-turbine findings from the VERTEX study,[11] here we extend them to the more complex case of overlapping wakes. The setup of the LES is described in Section 2. The simulation results are presented in Section 3, including wind speed deficit, added TKE, and temperature changes from single- and multi-turbine cases. The discussion in Section 4 focuses on the divergence/convergence of turbulent heat fluxes (Section 4.1), wake contraction (Section 4.2), and the dual nature of the wake (Section 4.3).

2 | NUMERICAL SIMULATION SETUP

We conduct idealized runs with WRF-LES-GAD version 3.9.1.1 without moisture, radiation schemes, and micro-physics. The Coriolis parameter is set to $0.911 \times 10^{-4}\ s^{-1}$, which corresponds to 38.78° N, where the VERTEX field campaign was located.[9]

2.1 | Computational domains

Two nested computational domains are used, with the domain with smaller grid spacing centered and one-way-nested within the outer domain (Figure 1). The horizontal grid spacing is 15 m for the outer domain and 5 m for the inner domain (Table 1), following Mirocha et al.[24] To better resolve the near-ground turbulent fluxes, we maximize the number of grid points below the rotor by setting Δz of the first vertical level to 2.5 m and then stretching it by 10% per level until 35 m. Then, Δz is kept constant at 5 m from 35 to 200 m and stretched 5% per level to the model top (set to 617, 1555, and 1959 m for stable, neutral, and unstable simulations, respectively, Table 1). The time step Δt of the outer domain is 1/7 s while Δt of the inner domain is one third of that of the outer domain.

2.2 | Lateral and boundary conditions

For the outer domain, the lateral boundary conditions are periodic, while for inner domain the lateral boundary conditions are updated from the outer domain at every outer domain time step. To absorb the gravity waves, a Rayleigh damping layer is applied at the top of the domain, with a depth of 150 m for stable, 500 m for neutral, and 700 m for unstable conditions.[18,22,24,29] The surface boundary is closed by a wall model based on the Monin–Obukhov similarity[30] as follows for momentum shear stress:

$$\tau_{i3} = -\left(\frac{\kappa\sqrt{\widetilde{u_1}^2+\widetilde{u_2}^2}}{ln(z/z_0)-\Psi_M}\right)^2 \frac{\widetilde{u_i}}{\sqrt{\widetilde{u_1}^2+\widetilde{u_2}^2}}, \tag{1}$$

and for surface heat flux:

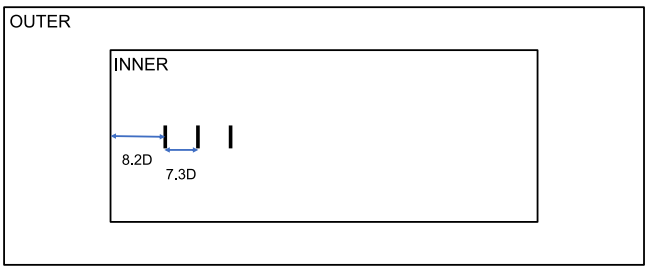

FIGURE 1 Layout of the computational domains. For the NOTURB case, no turbines are present; for the ONETURB case, only the left-most turbine is present; and for the ROW case, all three turbines are present. The dimensions and other details are listed in Table 1.

TABLE 1 Details of the computational domains.

		Outer	Inner			Outer	Inner
N_x		360	720	L_x (m)		5400	3600
N_y		120	240	L_y (m)		1800	1200
N_z	S	75		L_z (m)	S	617	
	N	96			N	1555	
	U	101			U	1959	
Δx (m)		15	5	Δz (m)		5 (across rotor)	

Note: N_x, N_y, and N_z are the number of grid points in the x (streamwise), y (spanwise), and z (vertical) directions; L_x, L_y, and L_z are the domain lengths in x, y, and z; Δx is the streamwise grid spacing (same as the spanwise Δy); Δz, the vertical level spacing, starts at 2.5 m, then stretches by 10% per level to 35 m, is constant at 5 m from 35 to 200 m (across the rotor), and then stretches by 5% per level to the model top L_z. "S" is for stable conditions, "N" for neutral, and "U" for unstable.

$$q_3 = \frac{u_* \kappa(\theta_{SK} - \tilde{\theta})}{ln(z/z_0) - \Psi_H}, \tag{2}$$

where $\widetilde{u_i}$ and $\tilde{\theta}$ are the resolved velocity and temperature at the first grid points from the wall, κ is the von Karman constant (0.4), z is the height from the first point above the wall, z_0 is the surface roughness length (0.01 m), u_* is the friction velocity calculated at the first grid point from the LES results, θ_{SK} is the prescribed skin temperature (described shortly), and Ψ_M and Ψ_H are the stability functions[31,32]:

$$\Psi_M = \begin{cases} -4.8z/L & Stable, \\ 0 & Neutral, \\ 2ln\left(\frac{1+X}{2}\right) + ln\left(\frac{1+X^2}{2}\right) - 2tan^{-1}(X) + \frac{\pi}{2} & Unstable, \end{cases} \tag{3}$$

and

$$\Psi_H = \begin{cases} -7.8z/L & Stable, \\ 0 & Neutral, \\ 2ln\left(\frac{1+X^2}{2}\right) & Unstable, \end{cases} \tag{4}$$

where $X = (1 - 15z/L)^{1/4}$ and L the Obukhov length[30]

$$L = -\frac{u_*^3 \tilde{\theta}}{\kappa g q_3}, \tag{5}$$

where g is the gravity acceleration (9.81 m s^{-2}).

2.3 | One-layer surface slab model

For the prescription of θ_{SK}, a one-layer slab surface energy balance approach is used,[33] which relates the flux used by WRF-LES to calculate surface temperature changes to the combination of surface sensible heat flux and net radiation:

$$C_s \frac{\partial \theta_{SK}}{\partial t} = -\rho C_p (r_{net} - q_3), \tag{6}$$

where C_s is the corrected thermal capacity of the soil slab per unit area, ρ is the air density, C_p is the heat capacity of air, r_{net} is the net solar radiative heat flux, and the surface flux q_3 comes from Equation (2). Based on the radiometer measurements and surface temperature changes from the VERTEX field campaign, C_s is set to 1.6×10^6 J K^{-1}m^{-2} and r_{net} is set to -0.07 K m s^{-1} for stable conditions, 0 K m s^{-1} for neutral conditions, and $+0.07$ K m s^{-1} for unstable conditions. This combination gives a reasonable rate of surface temperature change under different stability conditions.

2.4 | Sub-grid scale fluxes

The sub-grid scale momentum fluxes are modeled using the eddy-viscosity approach:

$$\tau_{ij} = -2\nu_{SGS}\tilde{S}_{ij}, \tag{7}$$

where $\widetilde{S_{ij}}$ is the filtered strain rate and ν_{SGS} is the eddy viscosity. Instead of the common Smagorinsky closure with a constant Smagorinsky coefficient, ν_{SGS} is obtained by the Lagrangian-average scale dependent (LASD).[34]

The sub-grid scale heat flux is modeled as

$$q_j = -\frac{\nu_{SGS}}{Pr_{SGS}} \partial_j \tilde{\theta}, \tag{8}$$

where Pr_{SGS} is the sub-grid scale Prandtl number which is set to the WRF default (1/3).

2.5 | Initialization

To achieve the same wind speed and direction at hub height—around 9 m s^{-1} from the west—under the three stability conditions, it is necessary to initialize WRF-LES with a different geostrophic wind for each stability, due to the different wind shear in the three cases from the Ekman spiral effect. The initial conditions for the streamwise and spanwise horizontal wind components of the geostrophic wind (U,V), after a trial-and-error procedure, are (10.06, −4.81) m s^{-1} under stable conditions, (10.55, −3.60) m s^{-1} under neutral conditions, and (10.761, −2.92) m s^{-1} under unstable conditions throughout the domain. These settings led to the desired outcome except for the unstable case, in which the hub-height wind speed was slightly higher (10.31 m s^{-1}).

The LES in the outer domain were spun up for some time to balance the solution with the geostrophic wind speed: 10 h for the stable, 13 h for the neutral, and 14 h for the unstable case. After that, the inner domain was introduced and run from 10 to 14 h for the stable, 13 to 17 h for the neutral, and 14 to 20 h for the unstable case. Average statistics were collected 1 h after the inner domain started for each run to allow turbulence spin-up in the inner domain.

The temperature profile is set to 297.3 K uniformly up to a different initial boundary layer height for each stability condition (200 m for stable, 500 m for neutral, and 800 m for unstable conditions). Above those heights, an inversion with a strength of 0.01 K m^{-1} is imposed for all stabilities. Small perturbations of ± 0.5 K were added to the initial temperature profile as a decreasing cubic function up to the initial boundary layer height to kick start turbulence.[24]

2.6 | The actuator disk model

The turbine used in this study is the PSU 1.5-MW PSU turbine[35] with hub height (H) of 80 m and diameter (D) of 77 m, in an effort to best mimic the Gamesa G90-2-MW turbine used in the VERTEX field campaign. As described in Mirocha et al,[24] the GAD model represents turbine wake effects by applying instantaneous forces to the three Cartesian velocity components. These forces result from airflow interactions with the turbine, which is parameterized as a disk representing the rotor swept area. Forces at each model grid point within the disk are calculated using lookup tables for the turbine lift and drag coefficients, as functions of radial distance from the hub, rotation rate of the turbine, wind speed, and angle of attack, the latter resulting from the flow angle relative to the blade orientation, which includes both pitch and twist. The forces are then averaged over the disk area, and smoothed in the axial direction using a Gaussian kernel with a standard deviation equal to the streamwise grid size Δx.[24]

2.7 | Simulations

Three simulations for each stability condition were conducted:

- NOTURB: Control cases with no turbines, one for each atmospheric stability conditions (stable, neutral, and unstable).
- ONETURB: Single wind turbine cases to investigate single wake effects under the three stability conditions, with a wind turbine placed in the domain at 630 m (approximately 8.2D) from the inlet of the inner domain and centered laterally (Figure 1).
- ROW: Multiple wind turbine cases to investigate overlapping wakes under the three stability conditions, with three turbines placed in a row in the inner domain and centered laterally. The first turbine is located at 630 m from the inlet of the inner domain, and the second and third turbine are aligned streamwise with a spacing of 7.3 D (Figure 1).

3 | RESULTS

3.1 | Precursor runs (NOTURB)

Starting with wind speed first from the NOTURB simulations (Figure 2A), we note that, although the initial magnitude of the geostrophic wind is the same for the three stability conditions (11.15 m s^{-1}), the resultant wind speed at hub height is different, due to the different wind shear.[18] The strongest hub-height wind occurs in the unstable case (over 10 m s^{-1}), since it has the least wind shear near the hub and the largest friction velocity (0.53 m s^{-1} vs. 0.47 and 0.36 m s^{-1} for neutral and stable, respectively), while the hub-height wind speed of the stable and neutral cases

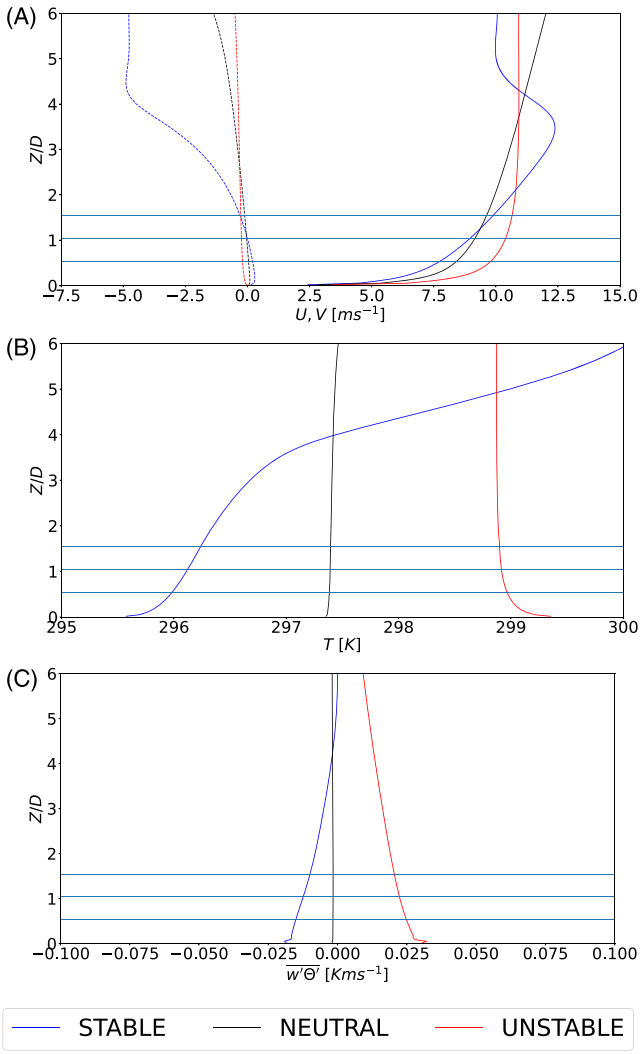

FIGURE 2 Vertical profiles, under stable (blue), neutral (black), and unstable (red) conditions and without wind turbines (NOTURB run), of time- and horizontally averaged: (A) wind speed components U (solid) and V (dashed); (B) potential temperature Θ; and (C) turbulent heat flux $\overline{w'\theta'}$. The three blue lines refer to the hub and the tips of the turbine.

TABLE 2 Scaling parameters for the three stability cases based on the NOTURB simulations.

Stability	U_∞ (m s^{-1})	u_* (m s^{-1})	q_3 (K m s^{-1})
Stable	8.96	0.37	−0.016
Neutral	9.16	0.45	0.0
Unstable	10.31	0.54	0.025

are similar (around 9 m s^{-1}). The strongest shear in the lower boundary layer and a low-level jet are observed in the stable case, which is consistent with theory[36] and previous findings.[18] The Coriolis effect introduces strong wind veering in the stable case above the rotor. The lateral wind speed component V at the hub is generally negligible.

For potential temperature (Figure 2B), the lapse rate is positive and an inversion is observed well above the rotor at approximately $z/D = 4$ in stable conditions. Under neutral conditions, potential temperature is nearly constant across the whole boundary layer. In the unstable case, the super-adiabatic layer extends to the bottom tip of the rotor, followed by adiabatic conditions above it, consistent with typical convective conditions.[36]

For turbulent heat flux (Figure 2C), in non-neutral conditions, the heat flux is strongest near the ground and decreases with height throughout the boundary layer. The heat flux is stronger in magnitude in unstable than stable conditions, consistent with Stull.[36]

The results of the NOTURB runs are used to calculate all the scaling parameters for this study, from u_* to average hub-height wind speed (Table 2).

3.2 | Wind speed deficit

The wind speed deficit in the wake is obtained from the time-averaged wind speed data from the simulations with and without turbines as follows:

$$\Delta U(x,y,z) = \overline{U}(x,y,z) - \overline{U}_{NOTURB}(x,y,z), \tag{9}$$

where $\overline{U}(x,y,z)$ and $\overline{U}_{NOTURB}(x,y,z)$ are the time-average wind speed at point (x,y,z) from the LES simulations with turbines (ONETURB or ROW) and without turbines (NOTURB), respectively. Although this formulation is not consistent with field measurements, where it is not possible to measure the wind speed without the turbine at the same point as the wind speed with the turbine, it is preferred here to display the actual pointwise impact of the wake. To determine the actual wake width, we use the normalized wind speed deficit as follows:

$$\delta U = \delta U(x,y,z) = \frac{\Delta U(x,y,z)}{U_\infty}, \tag{10}$$

where U_∞ is the undisturbed, time- and spatially averaged hub-height wind speed from the NOTURB run (Table 2). We will refer to the wind speed deficit calculated using Equation (10) as "actual" because it is derived directly from the simulation results without any assumptions. The actual wake width is determined as the smallest spanwise distance from the hub where $\delta U \leq 0.025$.

Starting with the ONETURB results (Figure 3), the maximum deficit is generally at hub height for all stabilities, but the wake becomes shorter when the atmospheric stability changes from stable to neutral and then unstable. Under stable conditions, the wake length can be as long as 30D, while in unstable conditions it is shorter than 20D. These wake lengths are longer than generally acknowledged, as the typical distance at which a wake is expected to have fully recovered is 20D. This possibly excessive length could be due to idealizations of the model setup, which filters our heterogeneities in the forcing and the landscape that could accelerate the breakup of the wakes in the real environment.

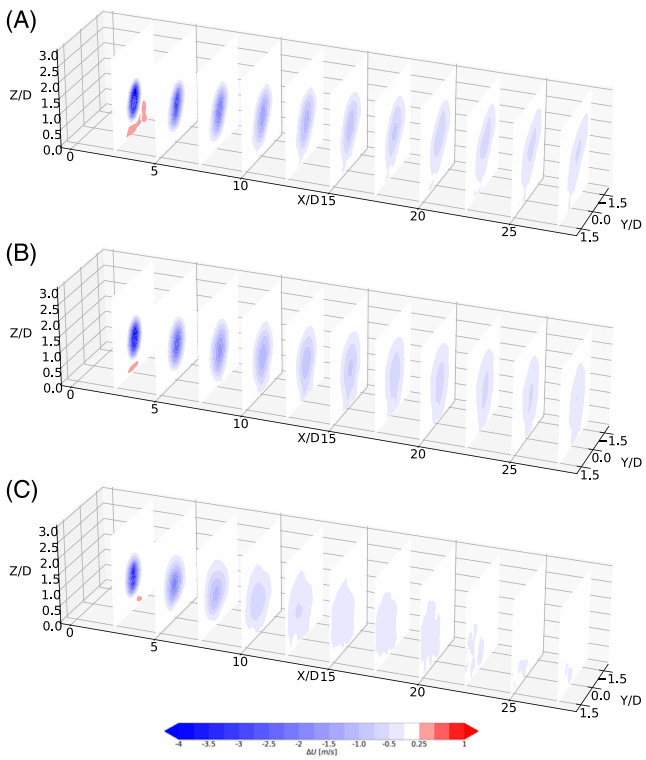

FIGURE 3 Contours of wind speed deficit (ΔU, m s^{-1}) from the ONETURB run for (A) stable, (B) neutral, and (C) unstable conditions.

Under stable and neutral conditions, the wake expands almost the same in the horizontal as in the vertical, reaching its maximum diameter of 2D between 12D and 15D. Then, interestingly, the wake stops growing and appears to actually contract (i.e., its diameter decreases rather than increasing further downstream until $\delta U \leq 0.025$). In unstable conditions, the wake expands more horizontally than vertically, contrary to previous studies[37]; the wake starts shrinking around 10D, and by 12D, it is barely detectable from the background. Although no study to date has reported a simulated or observed wake that stops expanding, we have found evidence of this in the lidar field measurement study by Iungo et al.[38] We will examine this issue further at the end of this section and in Section 4.2.

Under stable conditions (Figure 3A), the lateral stretch of the wake is evident, due to the slightly negative V-component above hub height that causes a clockwise wind veering, consistent with previous studies.[18,39]

For stable and neutral conditions (Figure 3A,B), a slight acceleration of the flow is found below the wake in the near wake (<3D), which is consistent with the findings of Xie and Archer.[18] The slight acceleration—or negative deficit—is basically negligible under unstable conditions, possibly because the higher background turbulence in unstable conditions tends to prevent its formation. The presence of this weak "jet" below the rotor in neutral and stable conditions is consistent with some observational studies, such as CWEX,[40] which found an increase in wind speed near the ground in the near wake under stable conditions and attributed this "overspeeding" to "perturbation pressure fields around each turbine."

The wake touches the ground (i.e., wake "touchdown") at about 15D under stable conditions (Figure 3A), while under neutral and unstable conditions the wind speed deficit already interacts with the ground at 10D (Figure 3B,C). The touchdown of the wake is consistent with the VERTEX findings of reduced wind speed near the ground described in Archer et al[9] and Wu and Archer,[11] although the magnitude of the simulated wind speed reduction is smaller than that observed in VERTEX, which was around 10% to 15%.

The shapes of the overlapping wakes from the ROW run (Figure 4) are similar to those of a single turbine, except all the wakes are longer and wider. Under stable conditions (Figure 4A), the wake stretches laterally and keeps growing until about 15D, after which it contracts. Under neutral conditions (Figure 4B), the wake contraction starts at about 15D as well. For unstable conditions (Figure 4C), the overlapping wake starts shrinking at 12D.

We note that the magnitude of the maximum wind speed deficit is about the same in the ONETURB and the ROW runs (Figures 3 and 4) for all stabilities, suggesting that the maximum wind speed deficit is not an additive property, but rather an intrinsic property related to the wind turbine spacing. As such, it is not enhanced much as more wind turbines are added, as long as their spacing remains the same. This will not be the case for TKE, as described next.

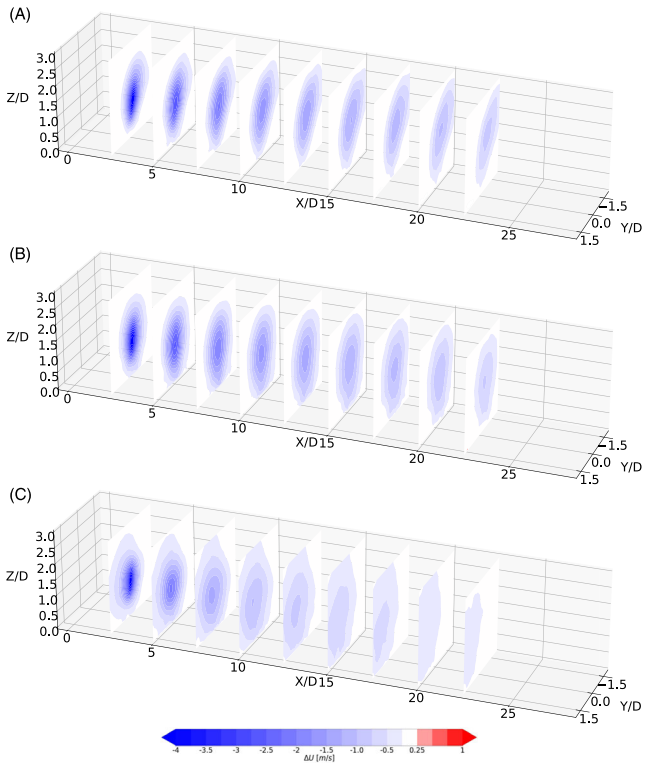

FIGURE 4 As in Figure 3, but from the ROW run (downwind of the third turbine).

3.3 | Added TKE

The added TKE (ΔTKE) is obtained from the TKE from the simulations with and without turbines as follows:

$$\Delta TKE(x,y,z) = TKE(x,y,z) - TKE_{NOTURB}(x,y,z). \tag{11}$$

For all three stability conditions, ΔTKE is enhanced across the rotor area and expands both horizontally and upward, but not much downward (Figures 5 and 6). Most TKE is added near and above the top tip under all stability conditions, which is consistent with previous studies.[18,41]

Unlike the wind speed deficit, which reaches the ground, the enhanced TKE stays elevated (no touchdown) and above the bottom tip under all stability conditions in the single-turbine case (ONETURB). Below the bottom tip, there is no enhancement of TKE. By contrast, a reduction of TKE is found below the bottom tip of the rotor starting at a downstream distance of 7D, most obvious under neutral and stable conditions (Figure 5A,B). The lack of enhancement of TKE below the rotor is consistent with the findings in VERTEX[9,11] and can be explained by the reduction of wind shear.

Under stable conditions, similar to the wind speed deficit, a strong lateral stretching of TKE occurs due to wind veering (Figure 5A). The added TKE is highest in stable conditions than any other case, with values exceeding 1.2 $m^2\ s^{-2}$ near the rotor top at 5D. For unstable conditions, TKE quickly spreads horizontally and vertically due to high turbulent mixing, which is in agreement with the study by Xie and Archer.[18] Less TKE is added in unstable conditions (at most 1.1 $m^2\ s^{-2}$ at 5D) and the reduced TKE below the rotor exhibits the lowest intensity and extent.

For overlapping wakes (Figure 6), the added TKE is significantly larger in magnitude compared to that in the single wake (Figure 5). The significantly larger added TKE is in contrast with the wind speed deficit, as the maximum deficit of overlapping wakes is of similar magnitude to

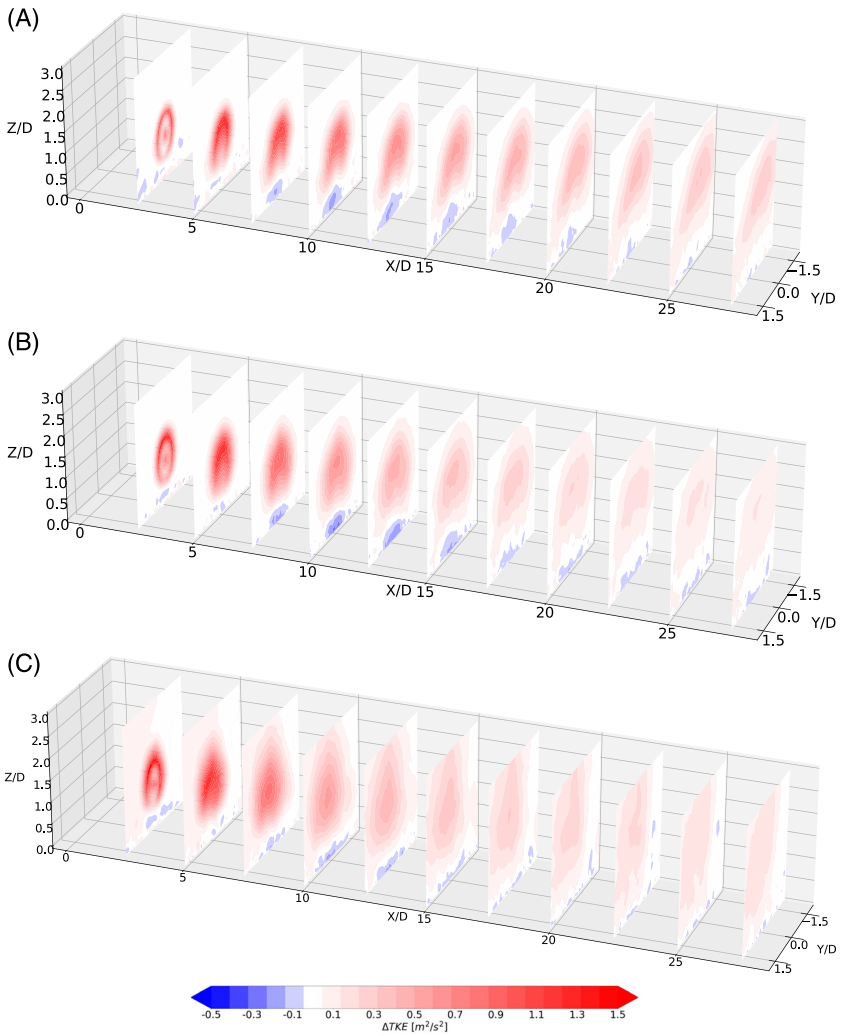

FIGURE 5 Contours of added TKE (ΔTKE, $m^2\ s^{-2}$) from the ONETURB run for (A) stable, (B) neutral, and (C) unstable conditions.

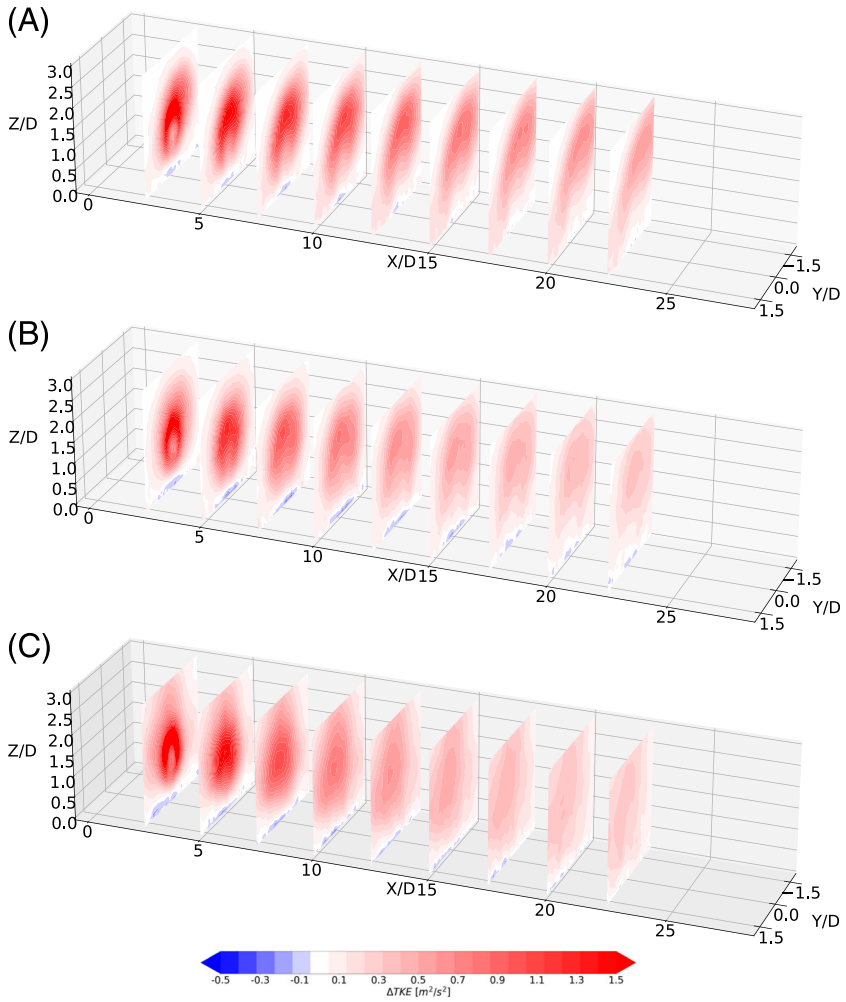

FIGURE 6 As in Figure 5, but from the ROW run (downwind of the third turbine).

TABLE 3 Location of the maximum TKE.

	Stable			Neutral			Unstable		
	X (D)	*Y* (D)	*Z* (D)	*X* (D)	*Y* (D)	*Z* (D)	*X* (D)	*Y* (D)	*Z* (D)
ONETURB	4.51	−0.03	1.50	3.54	−0.09	1.50	2.50	0.08	1.54
ROW	1.33	0.10	1.62	1.33	0.10	1.56	0.88	0.41	1.37

Note: *X*, *Y*, and *Z* are the streamwise distance from the turbine, spanwise distance from the hub, and height from ground, respectively, expressed as multiples of the diameter D.

that of a single wake (Figures 3 and 4). The expansion of the TKE is much stronger with multiple wakes compared to that of a single wake, and the added TKE extends below the rotor under all three stability conditions, although it only reaches the ground off the wake centerline in stable and neutral conditions after about 10D (Figure 6A,B).

The location of the maximum TKE is shown in Table 3. Under all stability conditions, the strongest TKE occurs near the top tip. The location of the maximum added TKE is different from the location of the maximum wind speed deficit, which occurs at the hub. Unlike the wind speed deficit, the expansion of TKE is always greater horizontally than vertically under all stability conditions, while the expansion of wind speed deficit is only greater in the horizontal under unstable conditions. If, instead of using the wind speed deficit, we use added TKE to identify the edges of the wake, then the wake has a much greater extent, reaching a width of 3D to 4D within a distance of 10D under all stabilities. The vertical extent is also noticeable, reaching 2D within a distance of 5D. This poses the interesting question: What exactly is a wind turbine wake? The question is not just philosophical, but practical and relevant. To understand the impacts of wakes on the environment, it is clearly necessary to identify the actual edges of the wakes. Does a wake really "end" by 30D streamwise, 2D spanwise, and 2D vertically, as the approach based on the wind

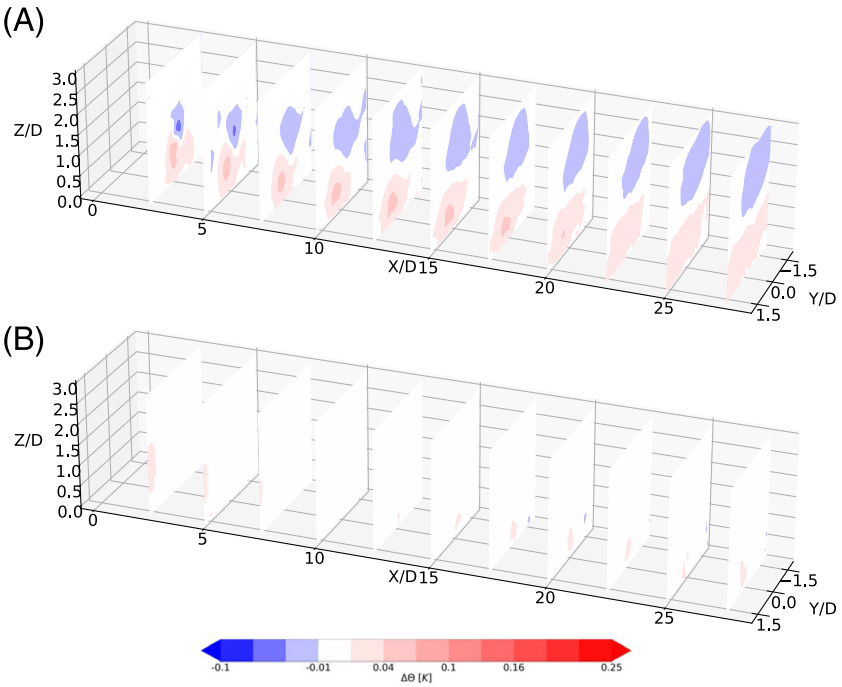

FIGURE 7 Contours of potential temperature difference ($\Delta\overline{\theta}$, K) from the ONETURB run for (A) stable and (B) unstable conditions.

speed deficit indicates? Or does it actually extend further downstream and upward and laterally, as the added TKE distribution suggests? More details will be discussed in Sections 4.2 and 4.3 to answer these questions on the dual nature of the wake.

3.4 | Wake-induced temperature changes

Starting with the single-turbine results from ONETURB, the wake under stable conditions (Figure 7A) causes a slight warming to a maximum of +0.05 K near the lower tip and cooling of up to −0.05 K near the top tip of the turbine. Although these changes are very small in magnitude, they are caused by real physical mechanisms, as described next. This pair of warming and cooling regions are not collocated vertically, but rather slanted in response to the clockwise rotation of the blades, which causes a counter-clockwise rotation of the air in the wake behind the rotor.[42,43] Because of the counter-clockwise flow rotation, the warming is found on the side with downward air motion and upward blade motion (the right side with respect to the incoming wind or northern side with $y > 0$) and the cooling on the side with downward motion of the blades and upward motion of the air. This distribution of the temperature effects is in agreement with previous studies[18] and VERTEX findings.[11]

Under unstable conditions, the temperature effect is small and negligible from a single wake (Figure 7B). The magnitude of the temperature changes induced by the wake of a single wind turbine in these WRF-LES results is smaller than that observed in VERTEX,[9,11] where the average changes near the ground were warming of the order of +0.2 K under stable conditions and negligible cooling under unstable conditions.

For overlapping wakes and under stable conditions (Figure 8A), the effect of warming below the rotor and cooling above is much stronger (up to +0.12 K) and spreads over a wider area both horizontally and vertically. In addition, the strongest warming shifts from near the lower tip for a single wind turbine wake to near the ground for overlapping wakes, while also shifting laterally towards the right of the centerline. Similarly, the strongest cooling occurs above the top tip but over a larger area compared to that of a single wake. The temperature effect in unstable conditions is still very small, but slight cooling is found near the ground (Figure 8B).

4 | DISCUSSION

Here, we demonstrate that the temperature effects, presented in Section 3.4, are caused by the changes in the vertical divergence of the turbulent heat flux (Section 4.1). We then further analyze the wind speed deficit results to show wake contraction within the context of the Gaussian similarity theory (Section 4.2).

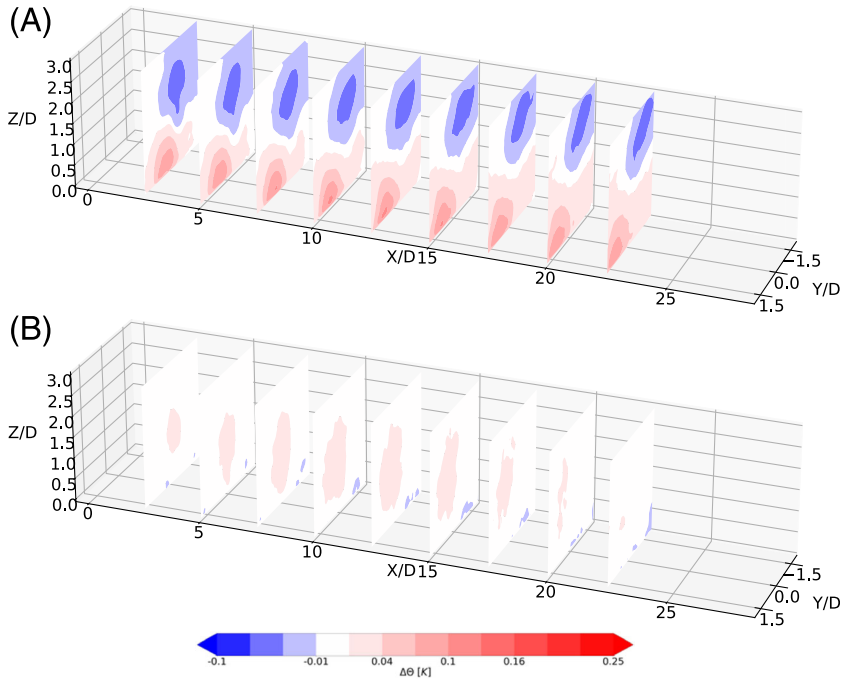

FIGURE 8 As in Figure 7, but from the ROW run.

4.1 | Divergence of turbulent heat flux

As proposed in Wu and Archer,[11] the physical mechanism that drives the temperature change near the ground is the convergence or divergence of turbulent heat flux below the rotor. The Reynolds-averaged energy equation can be written following eq. 3.4.5b in Stull[36]:

$$\frac{\partial \overline{\theta}}{\partial t} = \underbrace{-\overline{U_j}\frac{\partial \overline{\theta}}{\partial x_j}}_{\text{Advection}} \underbrace{-\frac{\partial \overline{u_j'\theta'}}{\partial x_j}}_{\text{Divergence}} + \nu\frac{\partial^2 \overline{\theta}}{\partial z} - \frac{1}{\overline{\rho} C_p}\frac{\partial Q}{\partial x_j} - \frac{L_v E}{\overline{\rho} C_p}, \tag{12}$$

in which the first term to the right of the equal sign is the advection, the second is the divergence of turbulent heat flux (with a minus sign to indicate that convergence causes warming), and the other three terms are viscous, radiation, and latent heat contributions, which we can ignore as a first approximation.

There are three terms each in the advection and divergence of turbulent heat flux terms, which are all normalized by $\frac{|q_3|}{D}$ (Table 2) as follows:

$$Adv_u = -\frac{\overline{u}\frac{\partial \overline{\theta}}{\partial x}}{\frac{|q_3|}{D}},\ Adv_v = -\frac{\overline{v}\frac{\partial \overline{\theta}}{\partial y}}{\frac{|q_3|}{D}},\ Adv_w = -\frac{\overline{w}\frac{\partial \overline{\theta}}{\partial z}}{\frac{|q_3|}{D}}, \tag{13}$$

$$Conv_u = -\frac{\frac{\partial \overline{u'\theta'}}{\partial x}}{\frac{|q_3|}{D}}, Conv_v = -\frac{\frac{\partial \overline{v'\theta'}}{\partial y}}{\frac{|q_3|}{D}}, Conv_w = -\frac{\frac{\partial \overline{w'\theta'}}{\partial z}}{\frac{|q_3|}{D}}. \tag{14}$$

The relationships between the warming patterns under stable conditions and the terms in Equations (13) and (14) can be appreciated by looking at Figure 9. For the single-turbine wake, a significant increase in the vertical convergence of the turbulent heat flux (positive $\Delta Conv_w$) is found below the rotor at 5D (Figure 9A), exactly where the warming was observed in Figure 7A. At steady state, the $Conv_w$ term is partially offset by the mean vertical advection Adv_w. Within the rotor area, the vertical convergence zigzags due to the hub effect. Above the top tip, it becomes negative, consistent with the cooling found earlier (Figure 7A), and it is balanced partly by the mean streamwise advection Adv_u.

From 10D (Figure 9B,C), the same patterns of increased $Conv_w$ below and decreased $Conv_w$ above the rotor are found, consistent with the warming/cooling distributions reported earlier, balanced in part by the mean streamwise advection Adv_u. For overlapping wakes under stable conditions (Figure 9D–F), the turbine-induced vertical convergence of turbulent heat flux becomes much larger in magnitude. The maximum induced convergence of turbulent heat flux is found near the ground and the effect of vertical advection is no longer significant.

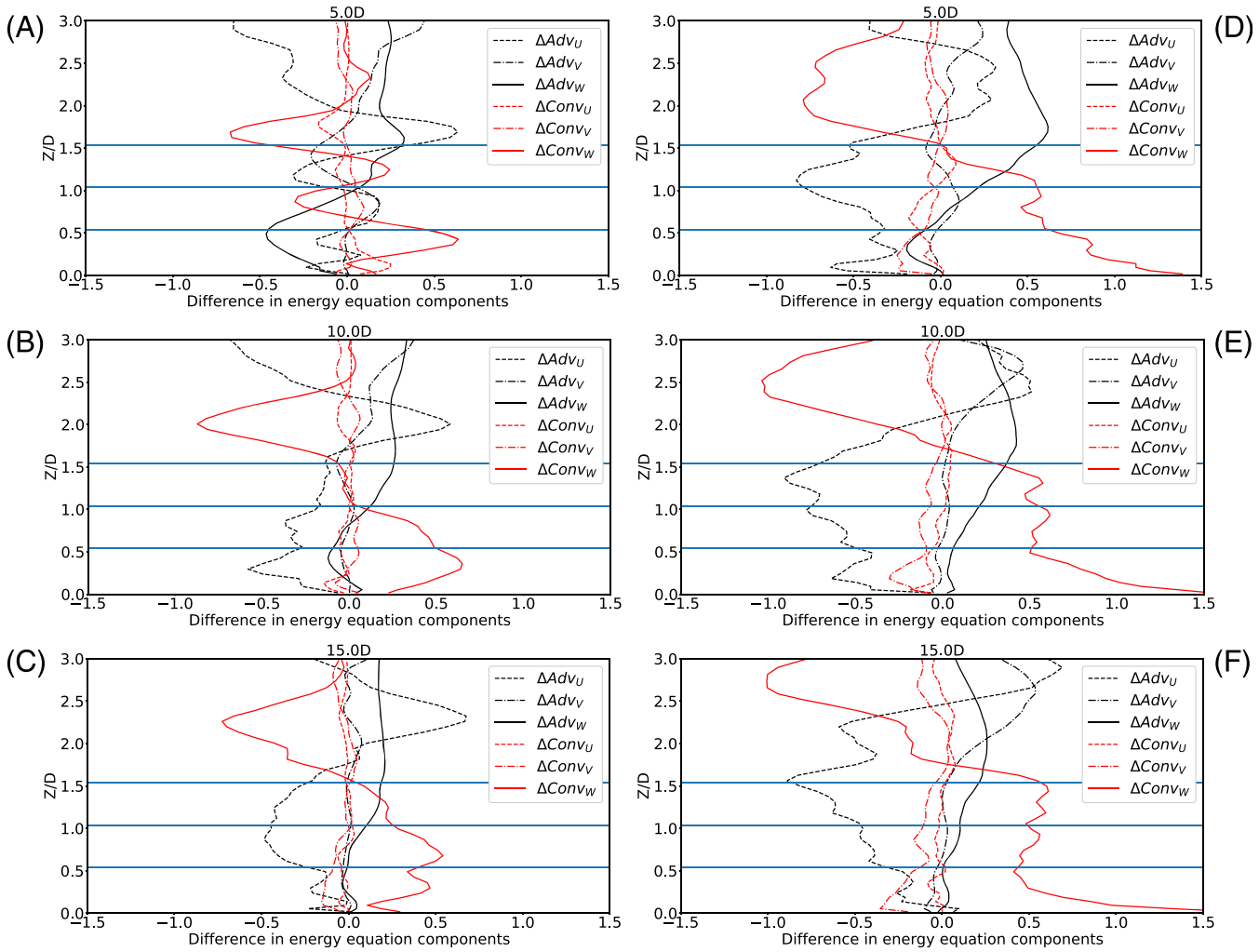

FIGURE 9 Vertical profiles of difference in potential temperature advection components Adv_x; Adv_y; Adv_z (Equation 13) and convergence components $Conv_x$; $Conv_y$; $Conv_z$ (Equation 14) spanwise-averaged ± 2D from the centerline at 5D (first row), 10D (second), and 15D (third) from the single turbine in run ONETURB (left) and from the last turbine in run ROW (right) for stable conditions. The three blue lines refers to the hub and the tips of the turbine.

For a single wake in unstable conditions (Figure 10A–C), the enhanced divergence caused by the wake is present (negative $\Delta Conv_w$), but it does not stand out among all the other components. For overlapping wakes (Figure 10D–F), the overall effect of the wind turbine is even weaker. Starting at 10D, the $Conv_z$ term is the dominant one below the rotor, although it is small, and it is negative, consistent with the modest cooling found there.

4.2 | Wake contraction

To improve our understanding of wake expansion and contraction, we compare the wake width as determined with the actual wind speed deficit, as done in the previous sections via Equation (10), with that determined via the traditional Gaussian fit. The Gaussian fit is often used in the literature[41,44–46] because it has the advantage that it tends to smooth out fluctuations in the wake field, like wake meandering or numerical noise, that may or may not be meaningful. We use the simulation results just to calculate the maximum wind speed deficit at each distance x downstream $\Delta U_{max}(x)$ and then a Gaussian fit to symmetrically distribute the deficit along each direction perpendicular to the main flow ξ, consistent with similarity theory, as follows:

$$\delta U^{GAUS} = \delta U^{GAUS}(x,\xi) = \frac{\Delta U(x,\xi)}{U_\infty} = \frac{\Delta U_{max}(x)}{U_\infty} e^{\frac{-\xi^2}{2\sigma^2}}, \tag{15}$$

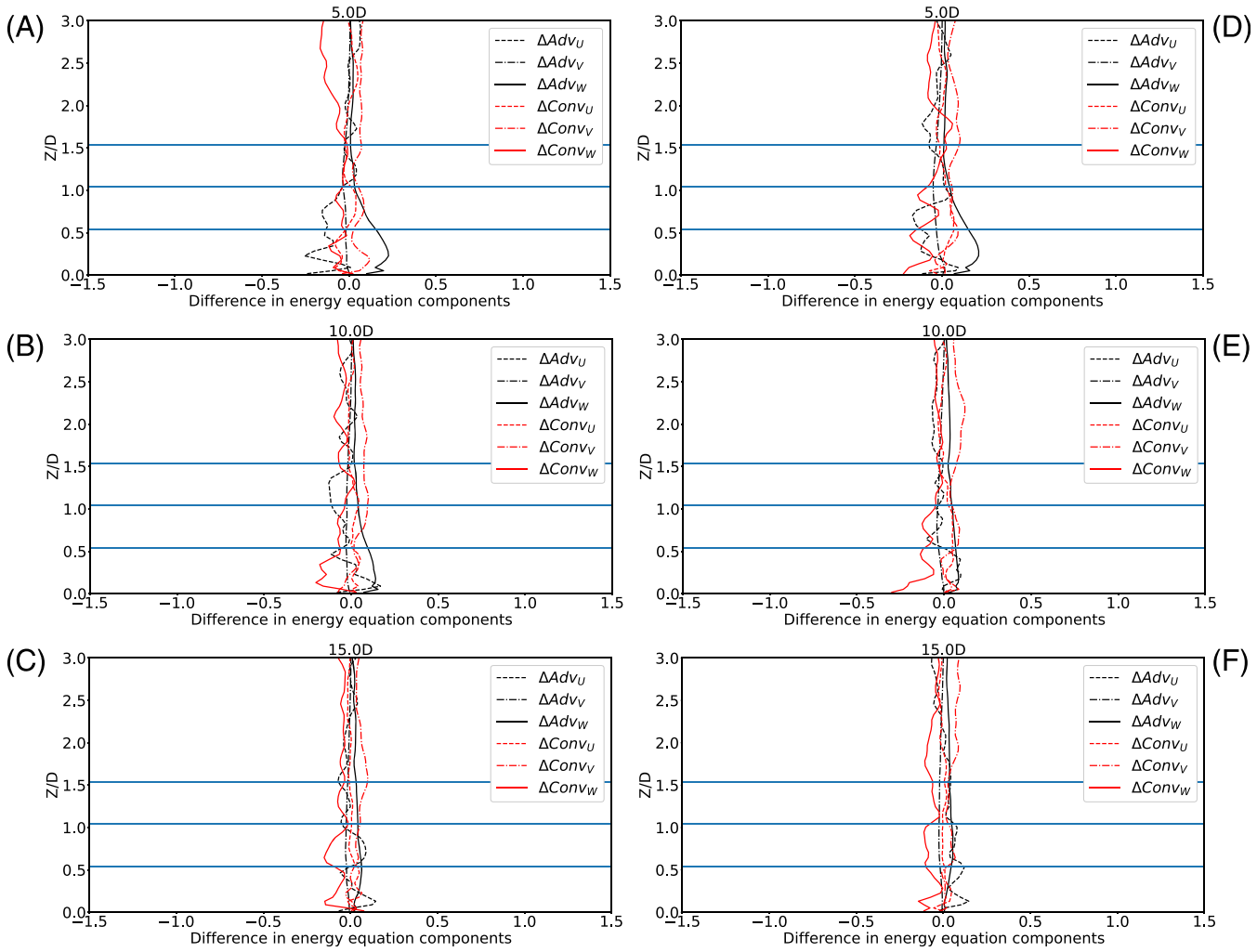

FIGURE 10 As in Figure 9, but for unstable conditions.

where ξ is either y (for lateral expansion) or z (for vertical expansion), ξ_* is the normalized distance from the point of the maximum deficit, either equal to $(y-y_{max})/D$ or to $(z-z_{max})/D$ for lateral or vertical expansions, $\Delta U_{max}(x)/U_\infty$ is the maximum normalized wind speed deficit at distance x from the turbine, and σ is the fitted standard deviation (initially set to 0.25). The wake width is defined as the width that includes 95% of the Gaussian-fitted normalized wind speed deficit (i.e., the 95% confidence interval or two standard deviations in this case); thus, the two edges of the wake around the centerline represent each 2.5% of the maximum normalized wind speed deficit at x or 5% combined.

The wake edges as identified using the Gaussian fit with the 95% confidence interval are shown with red crosses in Figure 11 in the horizontal plane at hub height and Figure 12 in the vertical at the central plane. Consistent with the findings of Abkar and Porté-Agel[41] and Xie and Archer,[18] the expansion of the wake is affected by atmospheric stability, with larger expansion rates as the atmosphere becomes more unstable. Starting with the ONETURB results (Figure 11A–C), the Gaussian fit shows an approximately linear expansion up to a certain point, at approximately 20D in stable, 15D in neutral, and 10D in unstable conditions, after which the Gaussian expansion rate remains constant or is even reduced, which confirms that the wakes do not expand indefinitely. The 5% actual wind speed deficit contours are well aligned with the red crosses up to approximately 10D, but then, the red crosses diverge, as the Gaussian assumption predicts a constant expansion, while the simulation results indicate that the wake stops expanding and starts to actually shrink at approximately the same distance at which the Gaussian fit stopped being linear (around 20D for stable, 15D for neutral, and 10D for unstable).

As the atmosphere becomes more unstable, the horizontal wake recovery is faster, meaning that the wake appears to end at about 30D in stable and neutral conditions, but at 15D in unstable. For overlapping wakes (Figure 11D–F), the Gaussian expansion rate at hub height is not found to be larger compared to that of a single wake, except in unstable conditions, for which the wake is also longer.

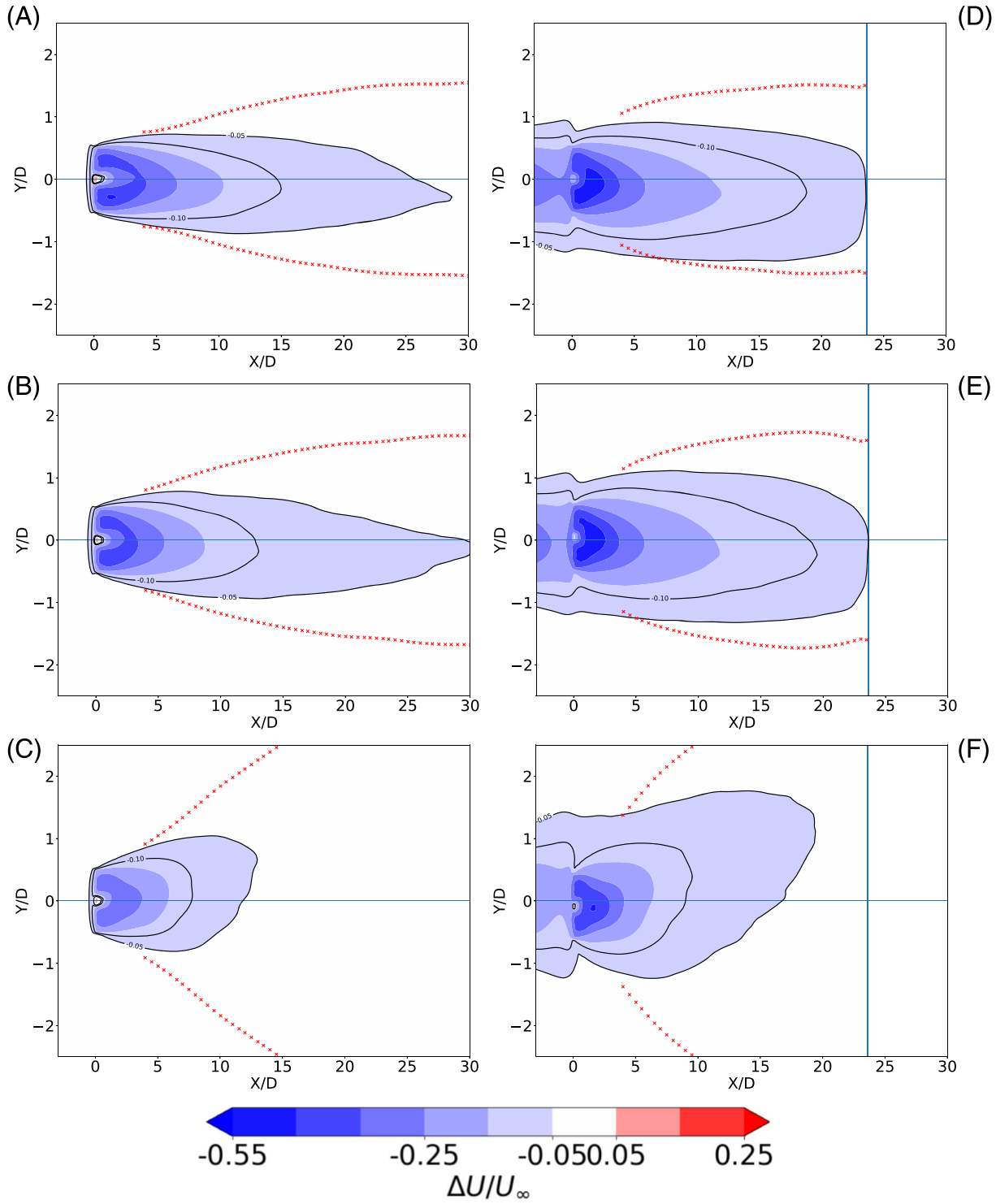

FIGURE 11 Contours of normalized time-averaged wind speed deficit $\Delta\overline{U}/U_\infty$ in the horizontal x–y plane at hub-height downwind of the single turbine in run ONETURB (left) and downwind of the third turbine in run ROW (right) under: (A,D) stable, (B,E) neutral, and (C,F) unstable conditions. The red crosses correspond to the 95% confidence interval of the normalized wind speed deficit fitted with the Gaussian distribution described in Equation (15). The end of the ROW domain is marked with a blue solid line. The horizontal blue line refers to the centerline of the hub.

Similar to the horizontal, the vertical expansion rate is also affected by atmospheric stability, with more expansion under neutral conditions (Figure 12). For a single wind turbine, the wake, as determined by the Gaussian fit, reaches the ground at about 12D for stable (Figure 12A), 8D for neutral (Figure 12B), and 10D for unstable (Figure 12C) conditions. For overlapping wakes, the wake hits the ground closer to the turbine than in the single-turbine case (Figure 12D–F), at approximately 5D for stable, 3D for neutral, and 5D for unstable conditions.

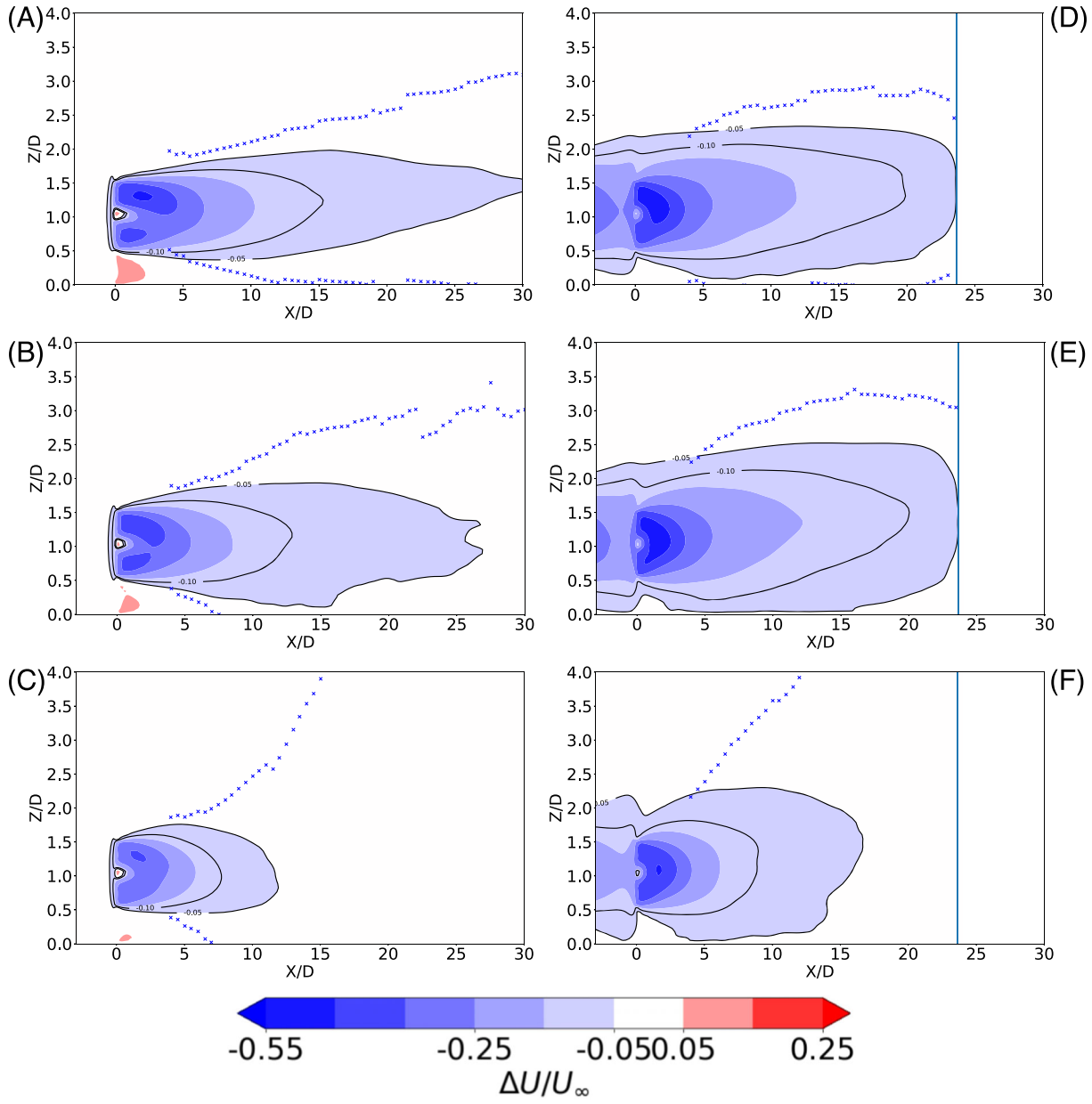

FIGURE 12 Same as in Figure 11 but in the vertical x–z central plane. The blue crosses correspond to the 95% confidence interval of the normalized wind speed deficit fitted with the Gaussian distribution described in Equation (15).

To better appreciate the differences in wake behavior when using the Gaussian fit versus the actual wind speed deficit, Figure 13 shows the wake edges in the horizontal and in the vertical as obtained with both methods. A linear fit for the Gaussian wake width is performed within $\pm$ 7.8D spanwise from the hub and to a distance downstream such that the normalized wind speed deficit is 5%.

In stable and neutral conditions, for both single and overlapping wakes, the expansion of the wake is almost the same in the horizontal and in the vertical, regardless of which method is used to detect the edges. In unstable conditions, however, the horizontal expansion rate (0.28 for single and 0.37 for overlapping wakes) is about double the vertical (0.14 for single and 0.23 for overlapping wakes) if the Gaussian fit is used. By contrast, the literature suggests that the expansion rate in the vertical should be larger than in the horizontal under unstable conditions.[18,41]

Another important confirmation is that the expansion of the wake, as determined with the wind speed deficit, is stability-dependent, meaning that it grows wider as the atmosphere becomes more unstable. For example, the Gaussian expansion rates change from 0.09 in stable to 0.11 in neutral to 0.28 in unstable conditions for single wakes in the horizontal. The wake expansion rates for single wakes change with stability also in the vertical (0.08, 0.11, and 0.14 for stable, neutral, and unstable conditions, respectively). The same patterns are found for overlapping wakes.

When we look at the actual wind speed deficit, however, the wake expansion is far from linear, with instead a gentler slope in the near wake, a maximum, and a gradual reduction in the far wake, both in the horizontal and in the vertical, for all stabilities. The exact position of the maximum

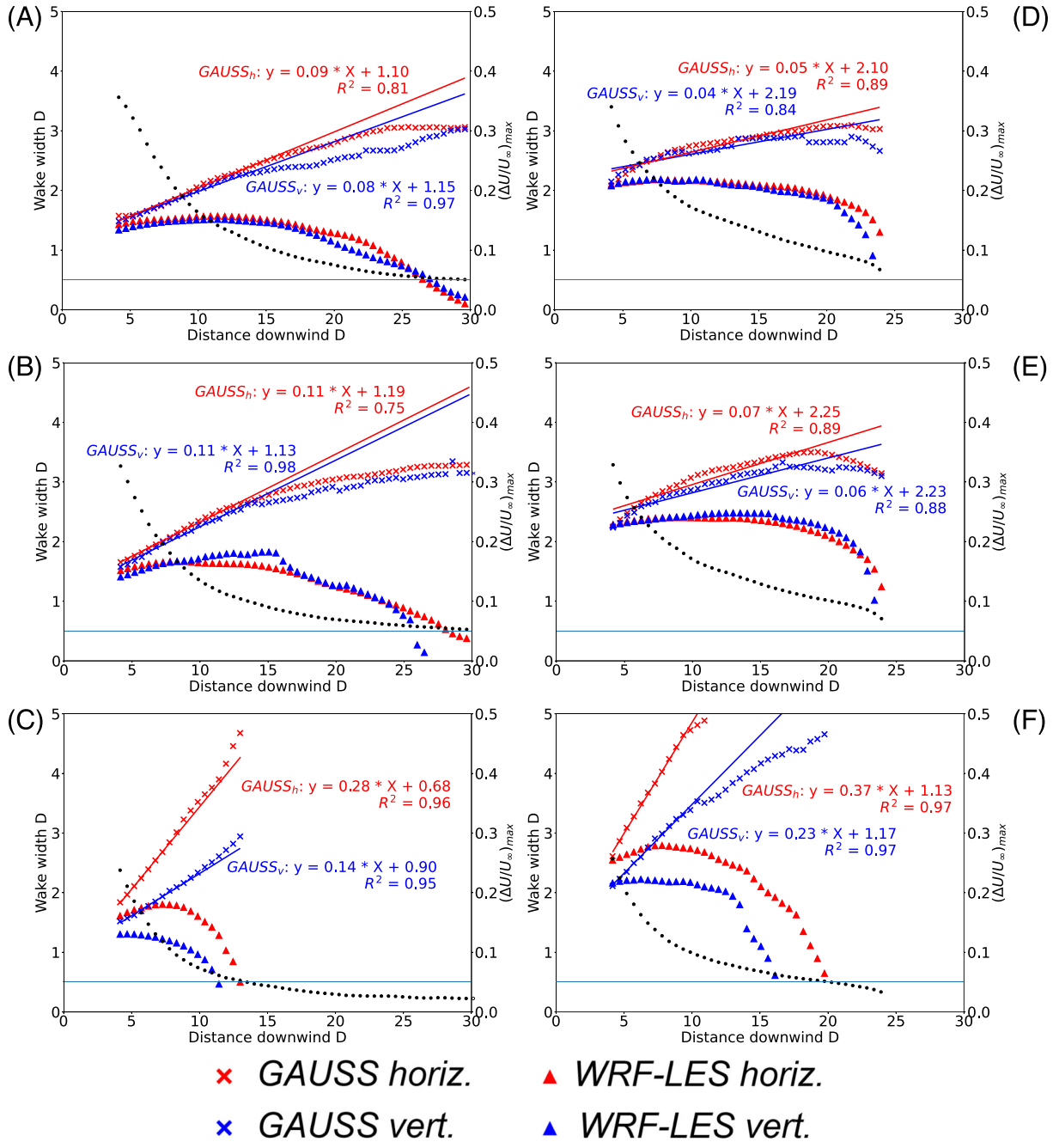

FIGURE 13 Wake expansion in the vertical (blue) and horizontal (red) based on wind speed deficit at hub-height downwind of the single turbine in run ONETURB (left) and downwind of the third turbine in run ROW (right) under: (A,D) stable, (B,E) neutral, and (C,F) unstable conditions. The 5% actual deficit and the 95% fitted Gaussian deficit (Equation 15) are shown with triangles and crosses, respectively. The wake is assumed to have recovered when the maximum normalized wind speed deficit ($\Delta U_{max}(x)/U_\infty$, black circles, right axis) is at 5% (horizontal blue line)

and the slope of the expansion and contraction vary by stability and for single versus multiple wakes. For example, under stable conditions for a single wake (Figure 13A), the wake width as determined with the actual wind speed deficit (triangles) is basically identical in the horizontal and vertical and grows slowly until about 12D, at which point it reaches 1.5D, to then decrease to almost zero at 30D. By contrast, the Gaussian-fitted wake at 30D is largest and approximately 3D wide.

These results suggest that, to determine the wake edges based on the wind speed deficit, the Gaussian fit may not be the most appropriate tool because it improperly creates an ever-expanding wake, when in reality the wind speed deficit values at the wake edges are already well below the detection limit and/or the accuracy of modern instrumentation, such as lidars. To put this argument in perspective, consider that the typical lidar accuracy is 0.2–0.5 m s^{-1}. In our stable case, for which $U_\infty = 8.82$ m s^{-1} (Table 2), an actual wind speed deficit ΔU lower than

$5\% \times 8.82\,\mathrm{m\,s^{-1}} = 0.4\,\mathrm{m\,s^{-1}}$, used in Figure 13A to identify the wake edges, is barely distinguishable from the background even with a lidar accuracy of $0.2\,\mathrm{m\,s^{-1}}$.

4.3 | Dual nature

The wake edges can also be studied using added TKE, as opposed to the wind speed deficit, with the Gaussian fit. In this case, Equation (15) is modified as follows:

$$\delta TKE^{GAUS} = \delta TKE(x,\xi)^{GAUS} = \frac{\Delta TKE(x,\xi)}{U_\infty^2} = \frac{\Delta TKE_{max}(x)}{U_\infty^2} e^{\frac{-\xi^2}{2\sigma}}, \tag{16}$$

but in this case $\xi = y$, as added TKE does not follow a symmetric Gaussian distribution in the vertical.

The expansion of added TKE at the top tip (118 m), where the highest TKE is found (Figure 14), as determined by the Gaussian fit in Equation (16), also shows a semi-linear expansion up to 15D in ONETURB, similar to the wind speed deficit, but the horizontal expansion rate is larger compared to that of the wind speed deficit (compare Figure 14 to Figure 11). The expansion rate of added TKE is also affected by stability,

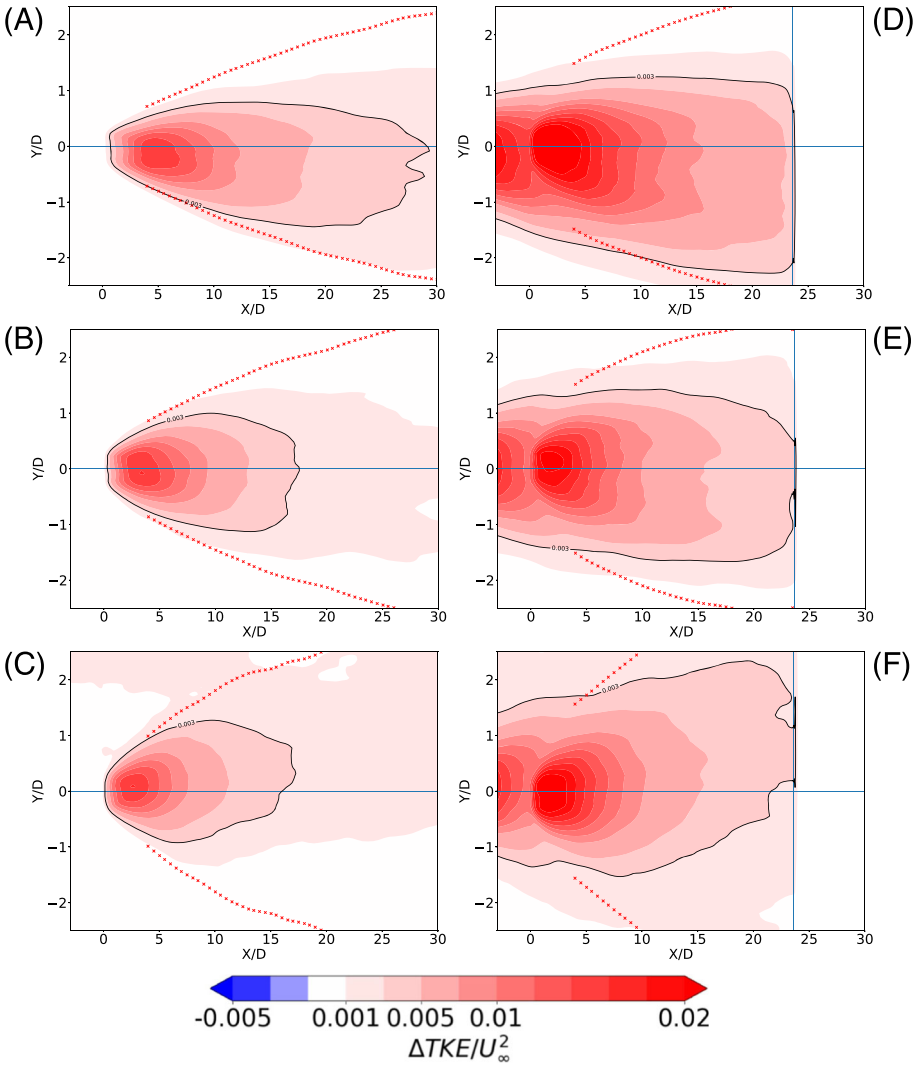

FIGURE 14 Contours of normalized time-averaged added TKE ($\Delta\overline{TKE}/U_\infty^2$) in the horizontal x–y plane at the top tip (118 m) downwind of the single turbine in run ONETURB (left) and downwind of the third turbine in run ROW (right) under: (A,D) stable, (B,E) neutral, and (C,F) unstable conditions. The red crosses correspond to the 95% confidence interval of the maximum added TKE fitted with the Gaussian distribution (Equation 16). The end of the ROW domain is marked with a blue solid line. The horizontal blue line refers to the centerline of the hub.

with the smallest expansion in stable conditions and largest expansion in unstable conditions, similar to the wind speed deficit. Similar expansion characteristics are also found in the ROW run with stronger magnitudes and larger wakes (Figure 14D–F).

We note that the 95% confidence Gaussian fit and the 5% actual added TKE are in better agreement than for wind speed deficit, up to about 10D for single and multiple wakes for all stabilities. To better compare the two, Figure 15 shows the wake width as determined by added TKE at the top tip. Since a confidence interval cannot be obtained for a skewed Gaussian, the Gaussian fit is not performed in the vertical for added TKE.

In the horizontal (red symbols and lines in Figure 15), the expansion of added TKE appears to be linear until the normalized added TKE reaches 0.003. This value has no particular physical meaning, but it seems to be associated with the end of the linear expansion of added TKE for all stabilities for both single and multiple wakes. In the horizontal, the expansion rate of added TKE is slightly higher with the 95% confidence interval of the Gaussian fit than with the 5% actual threshold, but the two are actually pretty close. By contrast, the wind speed deficit expanded at an excessively high rate with the Gaussian fit. This suggests that the Gaussian fit is better suited for added TKE than for the wind speed deficit

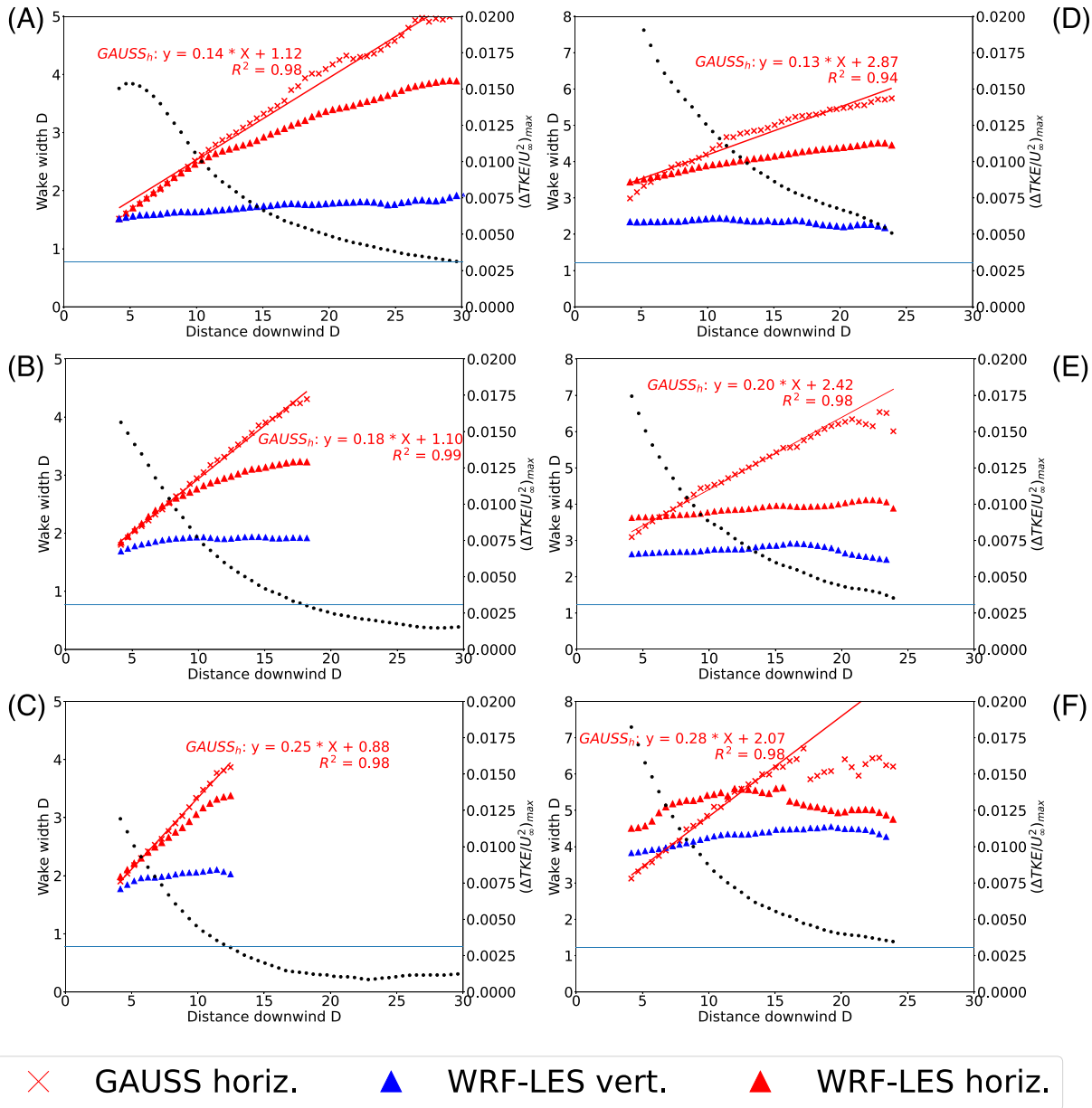

FIGURE 15 Wake expansion in the vertical (blue) and horizontal (red) based on added TKE at the top tip (118 m) downwind of the single turbine in run ONETURB (left) and downwind of the third turbine in run ROW (right) under: (A,D) stable, (B,E) neutral, and (C,F) unstable conditions. The 5% actual added TKE and the 95% fitted Gaussian added TKE (Equation 16) are shown with triangles and crosses, respectively. Note that the Gaussian fit cannot be used in the vertical because the vertical distribution of added TKE is not Gaussian. The wake is assumed to have recovered when the normalized maximum added TKE ($\Delta TKE_{max}/U_\infty^2$, black circles, right axis) is 0.003 (horizontal blue line)

(in the horizontal). The Gaussian expansion rates increase as the atmosphere becomes more unstable, with values of 0.14 for stable, 0.18 for neutral, and 0.25 for unstable for ONETURB (Figure 15A–C) and 0.13 for stable, 0.20 for neutral, and 0.28 for unstable for ROW (Figure 15D,E). The TKE expansion rates are larger for multiple wakes than for single wakes, except in stable conditions, where the rate is about the same (0.13–0.14) for both. These rates are about twice as large as those based on the wind speed deficit, which indicates that the wake turbulence expands much further horizontally than the wake wind speed deficit. In addition, the width and magnitude of added TKE in the horizontal are larger for overlapping wakes than for single wakes by a factor of two.

In the vertical (blue triangles in Figure 15), like for the wind speed deficit, the wake expansion based on added TKE is much more modest than in the horizontal and it does not increase with distance downwind, but rather remains at about the same value. This confirms that the wake-induced turbulence remains elevated and does not reach the ground. Like in the horizontal, the width and magnitude of added TKE in the vertical are also larger for overlapping wakes than for single wakes by a factor of two. Compared with the vertical wake width based on wind speed deficit, that based on TKE is actually rather similar for single and multiple wakes, with the only exception under unstable conditions, for which the vertical width based on TKE (2D for single and 4D for multiple wakes) is much larger than that based on wind speed deficit (1.5D for single and 2D for multiple wakes).

5 | CONCLUSIONS

This paper aims at better understanding the behavior of wind turbine wakes under different stability conditions, in terms of wind speed deficit and added TKE, and the subsequent changes in near-ground temperature caused by the wind turbines wakes.

To address these research questions, LES is performed under stable, neutral and unstable conditions. The main findings are as follows:

1. The wind turbine wake behaves differently in terms of wind speed deficit and added TKE, which is referred to as the "dual nature" of wind turbine wakes. The difference is observed in terms of the location and magnitude of the maximum, expansion rate, and touchdown.
2. The mechanism responsible for temperature changes near the ground is the vertical convergence/divergence of turbulent heat flux induced by the wake. Under stable conditions, the enhancement of the downward turbulent heat flux in the rotor area and the lack of change in surface heat flux cause convergence below the rotor, which induces warming. Vice versa, under unstable conditions, the enhancement of the (weak) upward turbulent heat flux in the rotor area and the lack of change in surface heat flux cause a weak divergence below the rotor, which induces a slight cooling. Overlapping wakes enhance the vertical convergence under stable conditions and the vertical divergence under unstable conditions, thus causing a slightly stronger warming and cooling.
3. The wakes do not expand indefinitely but eventually stop expanding, and actually contract, at different rates depending on atmospheric stability. For a single wake, the contraction starts when the normalized wind speed deficit is at around 10% and for overlapping wakes, the contraction starts at around 20%.

Because of the dual nature, we conclude that a wind turbine wake cannot be characterized by wind speed deficit only. The large majority of the literature has focused on analytical, numerical, and parameterized formulations of the wind speed deficit because wakes reduce wind speed, which directly impacts power production, the most important output of a wind farm. However, to study the impacts of wind farms on the environment, it is important to also correctly parameterize TKE, especially when investigating microclimate changes caused by wind turbine wakes,[16] because it is the wake turbulence that ultimately controls the convergence/divergence of the turbulent heat flux below the rotor. In addition, atmospheric stability is found to impact the expansion rate and shape of both the wind speed deficit and added TKE. The more unstable the atmosphere is, the more the expansion of wind speed deficit and TKE. With respect to the shape of the wake in terms of wind speed deficit, stable condition induce lateral stretching of the wake due to wind veering; neutral conditions cause a similar expansion of the wake in horizontal and vertical; and unstable conditions show more expansion in the horizontal than in the vertical.

The implication of these findings is that, in order to study wakes, whether with measurements in the field or with wind farm parameterizations in mesoscale simulations or with analytical wake loss models for power production, it is not sufficient to focus on the wind speed deficit alone. TKE is just as important, especially with respect to near-surface temperature, and yet it behaves differently from the wind speed deficit.

ACKNOWLEDGEMENTS

Funding for this research was provided by the National Science Foundation (Award n. 1564565). J.D.M.'s contributions were prepared by LLNL under Contract DE-AC52-07NA27344.

CONFLICT OF INTEREST STATEMENT

The authors report no conflicts of interest.

DATA AVAILABILITY STATEMENT

The LES data generated as part of this research are available upon request to the corresponding author.

ORCID

Sicheng Wu https://orcid.org/0000-0003-1718-067X
Cristina L. Archer https://orcid.org/0000-0002-7837-7575

PEER REVIEW

The peer review history for this article is available at https://www.webofscience.com/api/gateway/wos/peer-review/10.1002/we.2827.

REFERENCES

1. Baidya Roy S, Traiteur JJ. Impacts of wind farms on surface air temperatures. *Proc Natl Acad Sci U S A*. 2010;107(42):17899-17904.
2. Zhou L, Tian Y, Baidya Roy S, Dai Y, Chen H. Diurnal and seasonal variations of wind farm impacts on land surface temperature over western Texas. *Climate Dyn*. 2012;41(2):307-326.
3. Smith CM, Barthelmie RJ, Pryor SC. In situ observations of the influence of a large onshore wind farm on near-surface temperature, turbulence intensity and wind speed profiles. *Environ Res Lett*. 2013;8(3):34006.
4. Slawsky LM, Zhou L, Roy SB, Xia G, Vuille M, Harris RA. Observed thermal impacts of wind farms over northern Illinois. *Sensors (Switzerland)*. 2015;15(7):14981-15005.
5. Zhou L, Tian Y, Baidya Roy S, Dai Y, Chen H. Diurnal and seasonal variations of wind farm impacts on land surface temperature over western Texas. *Climate Dyn*. 2013;41(2):307-326.
6. Rajewski DA, Takle ES, Lundquist JK, et al. Crop wind energy experiment (CWEX): observations of surface-layer, boundary layer, and mesoscale interactions with a wind farm. *Bull Am Meteorol Soc*. 2013;94(5):655-672.
7. Rajewski DA, Takle ES, Lundquist JK, et al. Changes in fluxes of heat, H_2 O, and CO_2 caused by a large wind farm. *Agricult Forest Meteorol*. 2014;194:175-187.
8. Xia G, Zhou L, Freedman JM, Roy SB, Harris RA, Cervarich MC. A case study of effects of atmospheric boundary layer turbulence, wind speed, and stability on wind farm induced temperature changes using observations from a field campaign. *Climate Dyn*. 2016;46(7–8):2179-2196.
9. Archer CL, Wu S, Vasel-Be-Hagh A, et al. The VERTEX field campaign: observations of near-ground effects of wind turbine wakes. *J Turbulence*. 2019;20:64-92.
10. Moravec D, Barták V, Puš V, Wild J. Wind turbine impact on near-ground air temperature. *Renew Energy*. 2018;123:627-633.
11. Wu S, Archer CL. Near-ground effects of wind turbines: observations and physical mechanisms. *Monthly Weather Rev*. 2021;149(3):879-898.
12. Xia G, Zhou L, Minder JR, Fovell RG, Jimenez PA. Simulating impacts of real-world wind farms on land surface temperature using the WRF model: physical mechanisms. *Climate Dyn*. 2019;53(3–4):1723-1739.
13. Skamarock W, Klemp J, Dudhia J, et al. A description of the Advanced Research WRF version 3. NCAR/TN-4751STR, National Center for Atmospheric Research; 2008.
14. Fitch AC, Olson JB, Lundquist JK, et al. Local and mesoscale impacts of wind farms as parameterized in a mesoscale NWP model. *Monthly Weather Rev*. 2012;140(9):3017-3038.
15. Pan Y, Archer CL. A hybrid wind-farm parametrization for mesoscale and climate models. *Bound-Layer Meteorol*. 2018;168(3):469-495.
16. Archer CL, Wu S, Ma Y, Jiménez PA. Two corrections for turbulent kinetic energy generated by wind farms in the WRF model. *Monthly Weather Rev*. 2020;148(12):4823-4835.
17. Xie S, Ghaisas N, Archer CL. Sensitivity issues in finite-difference large-eddy simulations of the atmospheric boundary layer with dynamic subgrid-scale models. *Bound-Layer Meteorol*. 2015;157:421-445.
18. Xie S, Archer CL. A numerical study of wind-turbine wakes for three atmospheric stability conditions. *Bound-Layer Meteorol*. 2017;165(1):87-112.
19. Churchfield MJ, Lee S, Michalakes J, Moriarty PJ. A numerical study of the effects of atmospheric and wake turbulence on wind turbine dynamics. *J Turbulence*. 2012;13:N14.
20. Calaf M, Parlange MB, Meneveau C. Large eddy simulation study of scalar transport in fully developed wind-turbine array boundary layers. *Phys Fluids*. 2011;23(12):126603.
21. Calaf M, Meneveau C, Meyers J. Large eddy simulation study of fully developed wind-turbine array boundary layers. *Phys Fluids*. 2010;22(1):15110.
22. Lu H, Porté-Agel F. Large-eddy simulation of a very large wind farm in a stable atmospheric boundary layer. *Phys Fluids*. 2011;23(6):65101.
23. Lu H, Porté-Agel F. On the impact of wind farms on a convective atmospheric boundary layer. *Bound-Layer Meteorol*. 2015;157:81-96.
24. Mirocha JD, Kosović B, Aitken ML, Lundquist JK. Implementation of a generalized actuator disk wind turbine model into the Weather Research and Forecasting model for large-eddy simulation applications. *J Renew Sustain Energy*. 2014;6(1):13104.
25. Aitken ML, Kosović B, Mirocha JD, Lundquist JK. Large eddy simulation of wind turbine wake dynamics in the stable boundary layer using the Weather Research and Forecasting Model. *J Renew Sustain Energy*. 2014;6(3):33137.
26. Mirocha JD, Rajewski DA, Marjanovic N, et al. Investigating wind turbine impacts on near-wake velocity and turbulence characteristics using profiling lidar data and large-eddy simulations with an actuator disk model. *J Renew Sustain Energy*. 2015;7(4):43143.
27. Vanderwende B, Kosović B, Lundquist JK, Mirocha JD. LES and RANS representations of a small wind turbine array in WRF. *J Adv Model Earth Syst*. 2016;8(3):1376-1390.
28. Arthur RS, Mirocha JD, Marjanovic N, et al. Multi-scale simulation of wind farm performance during a frontal passage. *Atmosphere*. 2020;11(3):245.
29. Fitch AC, Lundquist JK, Olson JB. Mesoscale influences of wind farms throughout a diurnal cycle. *Monthly Weather Rev*. 2013;141(7):2173-2198.
30. Arya P. *Introduction to Micrometeorology*. 2nd ed.: Springer; 2001.
31. Paulson CA. The mathematical representation of wind speed and temperature profiles in the unstable atmospheric surface layer. *J Appl Meteorol Climatol*. 1970;9(6):857-861.

32. Deardorff JW. Numerical investigation of neutral and unstable planetary boundary layers. *J Atmospheric Sci*. 1972;29(1):91-115.
33. Dudhia J. A multi-layer soil temperature model for MM5. In: The Sixth PSU/NCAR Mesoscale Model Users' Workshop. National Center for Atmospheric Research; 1996:22-24.
34. Kirkil G, Mirocha J, Bou-Zeid E, Chow FK, Kosović B. Implementation and evaluation of dynamic subfilter-scale stress models for large-eddy simulation using WRF. *Monthly Weather Rev*. 2012;140(1):266-284.
35. Schmidt S. XTurb-PSU: a wind turbine design & analysis tool. https://www.aero.psu.edu/Faculty_Staff/schmitz/XTurb/XTurb.html; 2012.
36. Stull RB. *An Introduction to Boundary Layer Meteorology*. Springer; 1988.
37. Xie S, Archer CL. Self-similarity and turbulence characteristics of wind turbine wakes via large-eddy simulation. *Wind Energy*. 2015;18(10):1815-1838.
38. Iungo GV, Wu YT, Porté-Agel F. Field measurements of wind turbine wakes with lidars. *J Atmospheric Oceanic Technol*. 2013;30(2):274-287.
39. Churchfield MJ, Sirnivas S. On the effects of wind turbine wake skew caused by wind veer. *Wind Energy Symp*. 2018;2018:210029.
40. Rajewski DA, Takle ES, Lundquist JK, et al. Crop Wind Energy Experiment (CWEX): observations of surface-layer, boundary-layer, and mesoscale interactions with a wind farm. *Bull Am Meteorol Soc*. 2013;94(5):655-672.
41. Abkar M, Porté-Agel F. Influence of atmospheric stability on wind-turbine wakes: a large-eddy simulation study. *Phys Fluids*. 2015;27(3):035104.
42. Gebraad PMO, Teeuwisse FW, van Wingerden JW, et al. Wind plant power optimization through yaw control using a parametric model for wake effects—a CFD simulation study. *Wind Energy*. 2016;19:95-114.
43. Nouria R, Vasel-Be-Hagh A, Archer CL. The coriolis force and the direction of rotation of the blades significantly affect the wake of wind turbines. *Appl Energy*. 2020;277:115511.
44. Aitken ML, Lundquist JK. Utility-scale wind turbine wake characterization using nacelle-based long-range scanning lidar. *J Atmospher Oceanic Technol*. 2014;31(7):1529-1539.
45. Ge M, Wu Y, Liu Y, Yang XIA. A two-dimensional Jensen model with a Gaussian-shaped velocity deficit. *Renew Energy*. 2019;141:46-56.
46. Beck H, Kühn M. Reconstruction of three-dimensional dynamic wind-turbine wake wind fields with volumetric long-range wind doppler lidar measurements. *Remote Sens*. 2019;11(22):2665. https://www.mdpi.com/2072-4292/11/22/2665

How to cite this article: Wu S, Archer CL, Mirocha JD. New insights on wind turbine wakes from large-eddy simulation: Wake contraction, dual nature, and temperature effects. *Wind Energy*. 2024;27(11):1130-1151. doi:10.1002/we.2827